LETTER

Martian dust storm impact on atmospheric H$_2$O and D/H observed by ExoMars Trace Gas Orbiter

Ann Carine Vandaele[1]*, Oleg Korablev[2], Frank Daerden[1], Shohei Aoki[1], Ian R. Thomas[1], Francesca Altieri[3], Miguel López-Valverde[4], Geronimo Villanueva[5], Giuliano Liuzzi[5], Michael D. Smith[5], Justin T. Erwin[1], Loïc Trompet[1], Anna A. Fedorova[2], Franck Montmessin[6], Alexander Trokhimovskiy[2], Denis A. Belyaev[2], Nikolay I. Ignatiev[2], Mikhail Luginin[2], Kevin S. Olsen[6], Lucio Baggio[6], Juan Alday[7], Jean-Loup Bertaux[2,6], Daria Betsis[2], David Bolsée[1], R. Todd Clancy[8], Edward Cloutis[9], Cédric Depiesse[1], Bernd Funke[4], Maia Garcia-Comas[4], Jean-Claude Gérard[10], Marco Giuranna[3], Francisco Gonzalez-Galindo[4], Alexey V. Grigoriev[2], Yuriy S. Ivanov[11], Jacek Kaminski[12], Ozgur Karatekin[13], Franck Lefèvre[6], Stephen Lewis[14], Manuel López-Puertas[4], Arnaud Mahieux[1], Igor Maslov[2], Jon Mason[14], Michael J. Mumma[5], Lori Neary[1], Eddy Neefs[1], Andrey Patrakeev[2], Dmitry Patsaev[2], Bojan Ristic[1], Séverine Robert[1], Frédéric Schmidt[15], Alexey Shakun[2], Nicholas A. Teanby[16], Sébastien Viscardy[1], Yannick Willame[1], James Whiteway[17], Valérie Wilquet[1], Michael J. Wolff[8], Giancarlo Bellucci[3], Manish R. Patel[14], Jose-Juan López-Moreno[4], François Forget[18], Colin F. Wilson[7], Håkan Svedhem[19], Jorge L. Vago[19], Daniel Rodionov[2] & NOMAD Science Team and ACS Science Team[20]

Global dust storms on Mars are rare[1,2] but can affect the Martian atmosphere for several months. They can cause changes in atmospheric dynamics and inflation of the atmosphere[3], primarily owing to solar heating of the dust[3]. In turn, changes in atmospheric dynamics can affect the distribution of atmospheric water vapour, with potential implications for the atmospheric photochemistry and climate on Mars[4]. Recent observations of the water vapour abundance in the Martian atmosphere during dust storm conditions revealed a high-altitude increase in atmospheric water vapour that was more pronounced at high northern latitudes[5,6], as well as a decrease in the water column at low latitudes[7,8]. Here we present concurrent, high-resolution measurements of dust, water and semiheavy water (HDO) at the onset of a global dust storm, obtained by the NOMAD and ACS instruments onboard the ExoMars Trace Gas Orbiter. We report the vertical distribution of the HDO/H$_2$O ratio (D/H) from the planetary boundary layer up to an altitude of 80 kilometres. Our findings suggest that before the onset of the dust storm, HDO abundances were reduced to levels below detectability at altitudes above 40 kilometres. This decrease in HDO coincided with the presence of water-ice clouds. During the storm, an increase in the abundance of H$_2$O and HDO was observed at altitudes between 40 and 80 kilometres. We propose that these increased abundances may be the result of warmer temperatures during the dust storm causing stronger atmospheric circulation and preventing ice cloud formation, which may confine water vapour to lower altitudes through gravitational fall and subsequent sublimation of ice crystals[3]. The observed changes in H$_2$O and HDO abundance occurred within a few days during the development of the dust storm, suggesting a fast impact of dust storms on the Martian atmosphere.

Although dust is ubiquitous in the Martian atmosphere, global-scale dust storms (GDS) are relatively rare events[1,2] and only occurred twice in the last 17 years (in 2001 and 2007). The physical processes responsible for these phenomena are not yet fully understood, although several mechanisms have been proposed[3]. The ExoMars Trace Gas Orbiter (TGO) began orbiting Mars in October 2016 and started its observations in April 2018, just before the beginning of the 2018 GDS. The NOMAD and ACS instruments onboard TGO witnessed the onset and development of this GDS and its impact on water vapour abundance in the Martian atmosphere.

The 2018 GDS started on 30 May near the northern autumn equinox (at solar longitude $L_s \approx 185°$) and within a few weeks the planet was covered with atmospheric dust. Instruments on other Mars-orbiting and landed spacecraft also witnessed the storm's evolution (for example, PFS and VMC[9] onboard Mars Express, MARCI and MCS[10] on Mars Reconnaissance Orbiter and THEMIS[11] on Mars Odyssey). Observations by Curiosity[12] in Gale Crater indicated that the dust opacity rose from 0.65 on 7 June to 6.7 on 24 June, consistent with the values found by NOMAD and ACS, which observed dust opacity to increase by a factor larger than 10 (see Methods).

TGO has a two-hour orbit and can perform atmospheric measurements during two solar occultation events per orbit when the geometry is favourable. NOMAD and ACS measure the solar radiation spectrum, which is filtered by the atmosphere and from which the vertical distribution of atmospheric compounds—in particular, water vapour (both isotopologues, H$_2$O and HDO)—can be retrieved. The variation of atmospheric opacity with altitude can also be obtained directly from the decrease in the continuum part of the transmitted solar intensity, thus allowing the instruments to monitor the onset and further evolution of the GDS (Fig. 1).

In solar occultation mode, while the TGO-to-Sun line of sight sweeps tangent altitudes above the top of the atmosphere, the sampled line-of-sight optical depth is zero (that is, no attenuation of the solar signal). When the line of sight to the Sun transects the atmosphere, the line-of-sight optical depth gradually increases, owing to the presence of dust and ice particles, until the atmosphere becomes completely opaque at some tangent altitude. Here the transmittance drops to zero, which usually occurs because of increased dust presence in the lowermost part of the atmosphere or, in rarer cases, by crossing the planetary surface. Dust or cloud layers in the atmosphere cause local increases in optical depth, with the effect being most pronounced in the equatorial region (Fig. 1d–f). The characteristics of the individual vertical profiles of optical depth vary with latitude before, during and after the dust storm.

[1]Royal Belgian Institute for Space Aeronomy (IASB-BIRA), Brussels, Belgium. [2]Space Research Institute (IKI), Russian Academy of Sciences (RAS), Moscow, Russia. [3]Istituto di Astrofisica e Planetologia Spaziali (IAPS/INAF), Rome, Italy. [4]Instituto de Astrofísica de Andalucía (IAA), Consejo Superior de Investigaciones Científicas (CSIC), Granada, Spain. [5]NASA Goddard Space Flight Center, Greenbelt, MD, USA. [6]Laboratoire Atmosphères, Milieux, Observations Spatiales (LATMOS), UVSQ Université Paris-Saclay, Sorbonne Université, CNRS, Paris, France. [7]Department of Physics, Oxford University, Oxford, UK. [8]Space Science Institute, Boulder, CO, USA. [9]Department of Geography, University of Winnipeg, Winnipeg, Manitoba, Canada. [10]Laboratory for Planetary and Atmospheric Physics (LPAP), University of Liège, Liège, Belgium. [11]Main Astronomical Observatory (MAO), National Academy of Sciences of Ukraine, Kiev, Ukraine. [12]Institute of Geophysics, Polish Academy of Sciences, Warsaw, Poland. [13]Royal Observatory of Belgium, Brussels, Belgium. [14]School of Physical Sciences, The Open University, Milton Keynes, UK. [15]Geosciences Paris Sud (GEOPS), Université Paris Sud, Orsay, France. [16]School of Earth Sciences, University of Bristol, Bristol, UK. [17]Centre for Research in Earth and Space Science, York University, Toronto, Ontario, Canada. [18]Laboratoire de Météorologie Dynamique (LMD), CNRS Jussieu, Paris, France. [19]European Space Research and Technology Centre (ESTEC), ESA, Noordwijk, The Netherlands. [20]A list of participants and their affiliations appears at the end of the paper. *e-mail: a-c.vandaele@aeronomie.be
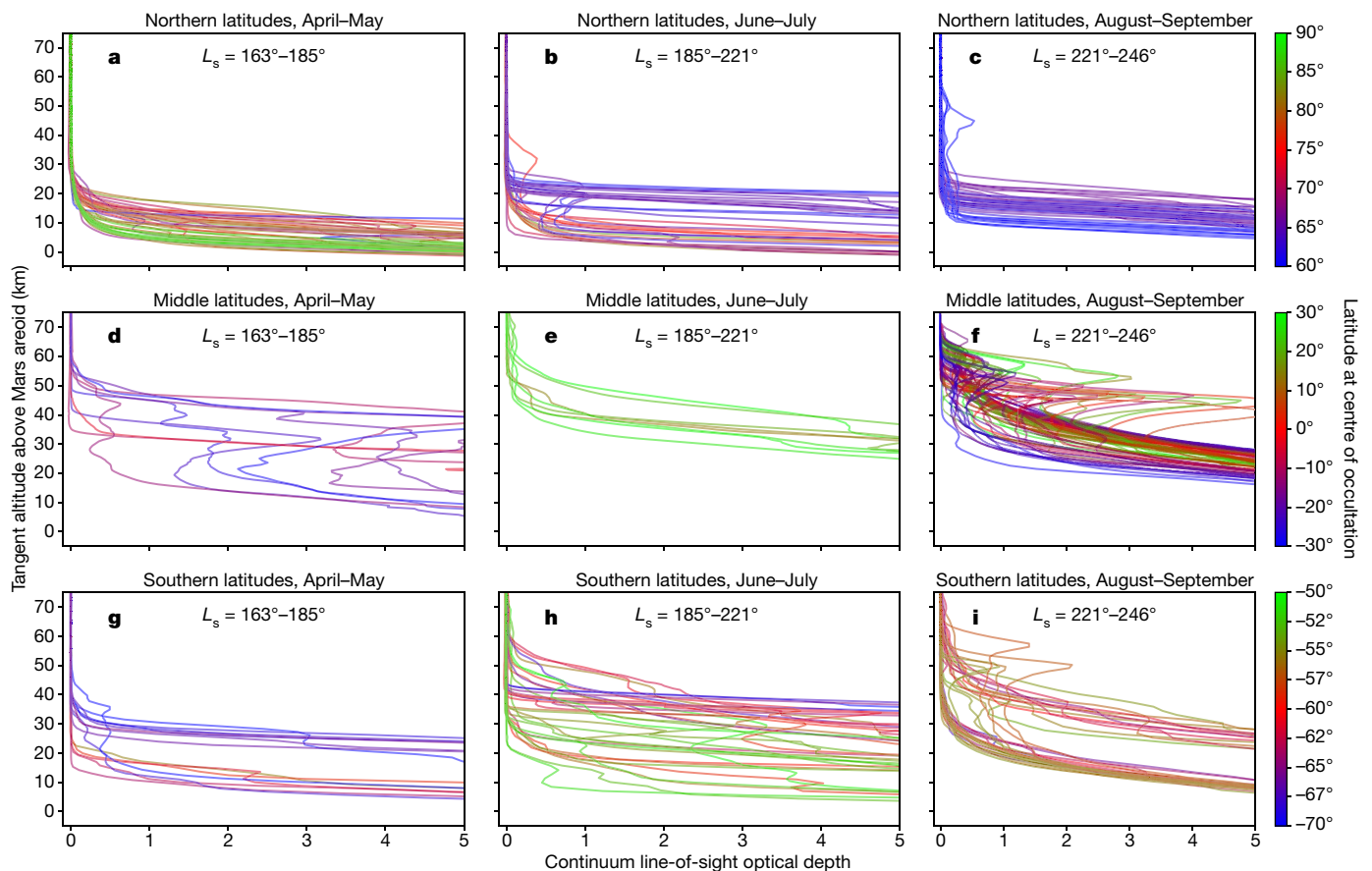
Fig. 1 | Evolution of dust/cloud extinction during the onset of the GDS.
a–i, Data obtained by the NOMAD Solar Occultation channel, from the first observations in April and May 2018 (**a**, **d**, **g**) to the August–September 2018 timeframe (**c**, **f**, **i**), spanning $L_s = 163°$–$246°$ (late northern summer to autumn). The data, which consist of 536 individual measurements, are split into three latitude bins, with the colour of the line indicating the latitude of each bin. The latitudinal coverage is dependent on the orbit and solar position, so the latitude ranges were selected on the basis of the data available: northern profiles for latitudes >60 °N (**a–c**), mid-latitude profiles for latitudes between −30° S and 30° N (**d–f**) and southern profiles for latitudes between −70° S and −50° S (**g–i**). In the early phase of the TGO mission, more solar occultations occurred near the northern pole, as is evident in the figures. Plotted here is the continuum line-of-sight optical depth versus the tangent altitude of the centre of the line of sight above the Mars reference areoid. The line-of-sight optical depth is inferred from the transmittance after the removal of atmospheric absorption lines. Diffraction order 121 was used for this study, covering the spectral range 2,720–2,740 cm^{-1}. Horizontal error bars are not shown here because they are very small: for a signal-to-noise ratio of 1,000, the 1σ error is 0.003 for an optical depth of 1 and 0.06 for an optical depth of 4.

The observations in Fig. 1a–c, made north of 60° latitude, indicate that the continuum line-of-sight optical depth remains low down to a tangent altitude of 10–20 km throughout the dust storm. The apparent increase with time of the tangent altitude at which the atmosphere becomes opaque is mainly a latitude effect, indicating that the GDS does not impact the northern latitudes much. From June onwards some features were observed at altitudes of 25–40 km that were not present before the dust storm; these could be layers of dust transported from lower latitudes.

In the middle latitudes (Fig. 1d–f), before the dust storm many layers were observed at around 40 km. Detached dust layers were previously identified on many occasions[13–15], and their existence has been explained by uplifting during strong convection processes[16–19]. Water-ice clouds may be responsible for some of the observed layers, as indicated by observations at other wavelengths and by previous investigations[20–22]. The layers disappeared during the dust storm, when the atmosphere was utterly opaque below 40 km because of high dust abundances. Water-ice clouds are expected to disappear owing to atmospheric warming during the dust storm[13].

Furthermore, Fig. 1g–i shows the impact of dust/ice clouds in the high southern latitudes, from the beginning of southern spring to the onset of the dusty southern summer season. During the GDS, dust ascended to higher altitudes, similarly to the situation in the middle latitudes but with more local variability.

On Mars, water vapour has a wide variety of effects on atmospheric photochemistry and climate. Its dissociation by sunlight into hydroxyl radicals controls the overall stability cycle of CO_2. Water exerts a strong influence as frost on the surface or as ice clouds in the atmosphere, leading to large departures from the otherwise dust-controlled radiative balance[3].

Here we present the first water vapour profiles at high vertical resolution (about 1 km), which extend from the planetary boundary layer up to about 80 km (Figs. 2 and 3a). In addition, we report the first measurements of the vertical profile of HDO (Fig. 3b). The first observations from TGO were carried out before the 2018 GDS, and the impact of the GDS on the vertical distribution of water vapour and HDO was monitored. The ACS observations shown in the figures were performed at high southern and northern latitudes, whereas the NOMAD profiles were obtained in northern mid-latitudes. During the northern autumnal season, when these measurements were carried out, previous column-integrated measurements[7,8] indicated a dry atmosphere at high latitudes caused by the developing seasonal polar cap in the North and its receding counterpart in the South. Temperatures are low enough to condense out CO_2 and as a consequence water vapour is also removed from the lower atmosphere by condensation into clouds and subsequent sedimentation[3]. The seasonal cap development therefore explains the very low water abundances in the lowest 20 km for the sub-polar profiles (Fig. 2). The profiles observed before the dust
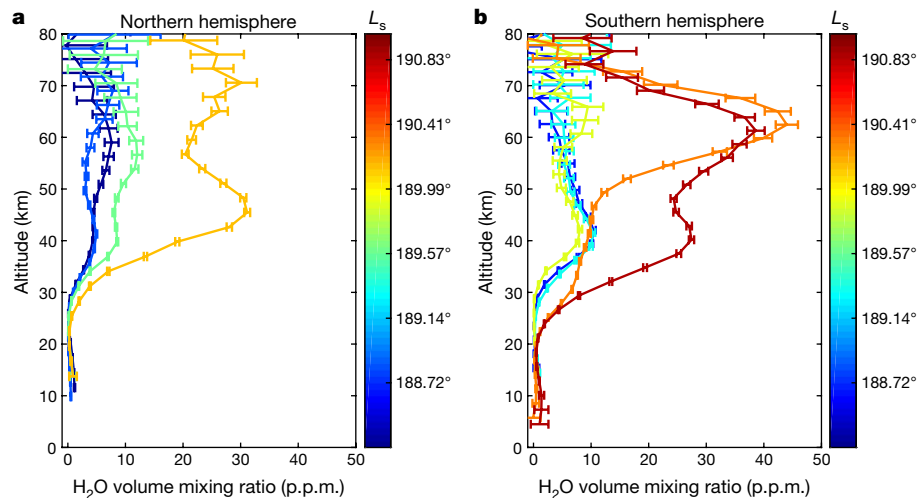
Fig. 2 | H$_2$O volume mixing ratio profiles observed by ACS NIR during the onset of the GDS. a, Northern latitudes. The L_s and latitude values are: 188.28°, 77.5° N (black); 188.75°, 76.4° N (blue); 189.41°, 74.8° N (green); and 189.90°, 73.8° N (yellow). **b**, Southern latitudes. L_s and latitude: 188.62°, 68.2° S (blue); 189.19°, 70.0° S (cyan); 189.67°, 71.3° S (yellow); 190.05°, 72.4° S (orange); and 190.50°, 73.8° S (red). Water abundances were deduced from ACS NIR observations (order 56, covering the 1.38-μm band, 7,225–7,300 cm^{-1}; the CO$_2$ density was measured in order 49, 6,320–6,390 cm^{-1}; see Methods). The uncertainty in the local number density is given by the covariance matrix of the solution error (as described in Methods).

storm indicate low abundances of water vapour above 60 km, with values below 10 p.p.m. and with large error bars. Profiles from the southern hemisphere are shown in Figs. 3a and 2b; they correspond to the southern summer season, with a lot of dust already present in the atmosphere before the GDS, explaining the cut-off at about 15 km. Northern hemisphere profiles were taken in more dust-free conditions and reach down to about 4 km.

Water profiles, of both H$_2$O and HDO, show a large enhancement in the middle atmosphere after the onset of the dust storm. The increase in water abundance is observed above 20 km, with water vapour being lifted upwards up to at least 80 km. Previous studies have reported a sharp decrease in the total water column in the equatorial region[7,8], which is indicative of redistribution of water vapour in a dust storm. Previous measurements[5] of water vapour profiles showed an increase in the atmospheric water content at high altitudes and latitudes, as confirmed by our data. This phenomenon has been also linked to an increase in the escape of hydrogen from Mars'

atmosphere[6,23]. What is remarkable in the observations presented here (Fig. 2), is that this enhancement occurs very fast, in the course of just a few days, during the onset of the dust storm (around 7–8 June, $L_s \approx 188°–190°$).

The observed changes in the distribution of atmospheric water reported here can be understood as resulting from a variety of processes. The higher abundance of dust heats large parts of the atmosphere because of the absorption of solar radiation by the dust particles. Dust absorption and the subsequent warming of the surrounding gas cause an expansion of the atmosphere, which leads to a redistribution of water vapour across a wider vertical range. The higher atmospheric temperatures at low and middle latitudes and the resulting higher thermal contrast between the equatorial and polar regions also strengthen the mean meridional circulation; this leads to an additional redistribution of water vapour across latitudes. Also because of the higher temperatures, fewer water-ice clouds are expected to be present during a dust storm. Under non-dust-storm conditions, the formation of clouds
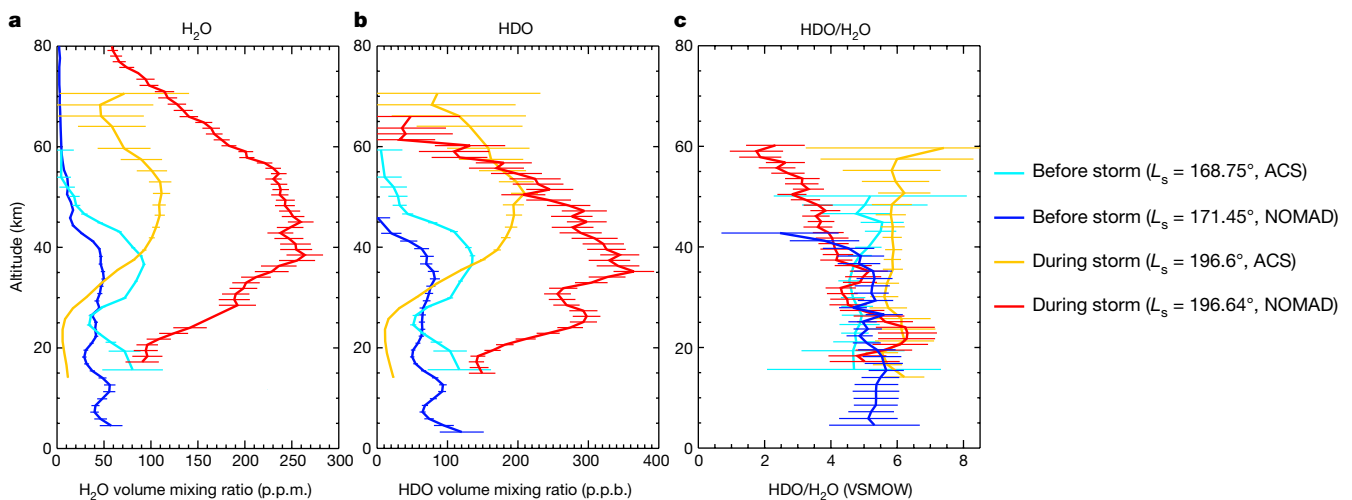

Fig. 3 | H$_2$O, HDO and D/H detections before and during the storm. a, NOMAD H$_2$O observations before the storm (blue, $L_s = 171.45°$ and latitude 43° N–68° N) and during the storm (red, $L_s = 196.64°$ and latitude 51° N–59° N), and ACS MIR observations before the storm (cyan, $L_s = 168.75°$ and latitude 39° S–43° S) and during the storm (yellow, $L_s = 196.64°$ and latitude 80° S–83° S). **b**, The corresponding HDO volume mixing ratio profiles. p.p.b., parts per billion. **c**, The D/H ratio, obtained for each of the H$_2$O and HDO observations. All errors are 1σ. VSMOW, Vienna standard mean ocean water reference value (312 p.p.m.).

confines water vapour to lower altitudes owing to the gravitational fall and subsequent sublimation of ice crystals. In addition, numerical modelling has demonstrated that solar heating of atmospheric dust can drive localized deep convection[17,18] and larger-scale ascent of dust layers[19], which would also transport water vapour to higher altitudes along with the dust. All of these processes that contribute to explaining the observed changes in the water vapour profiles have been quantitatively demonstrated by global circulation models and assimilation of water vapour data acquired in previous years on Mars[3,24–26]. For a more quantitative understanding of the 2018 GDS, more detailed modelling and assimilation studies that simulate the transition from normal to GDS conditions[3,24,25,27] will have to be performed, using dust constraints derived from instruments monitoring the GDS, including TGO instruments.

The fractionation between H_2O and HDO is an important process in planetary atmospheres. The deuterium/hydrogen (D/H) ratio is a marker of the evolution of the water inventory on Mars[28]. On Mars, the D/H budget is dominated by H_2O and HDO, which are the unique precursors of the escaping deuterium and hydrogen atoms above the exobase. HDO was previously measured from Earth as column-integrated abundances[29–31] and in situ[32] by the Mars Science Laboratory. NOMAD and ACS provide for the first time the capability to observe the vertical distribution of HDO simultaneously with water vapour, thereby providing key information on the fractionation processes that are expected to control the amount of hydrogen and deuterium atoms escaping to space[3]. H_2O and HDO are fractionated during photolysis and ice formation[33]. NOMAD observations (Fig. 3) reveal that the HDO density profiles during the pre-storm period exhibit a sudden decline at altitudes of 40–45 km, just below a layer of water-ice clouds (see Methods). ACS observations show this decrease to occur at 50 km but these data were taken at a different latitude, where the hygropause may be located at a different altitude. The HDO/H_2O ratio below 45 km is similar in both profiles: 4–6 VSMOW (Vienna standard mean ocean water). HDO is distinctly more abundant at high altitudes during the dust storm than before the storm. We suggest that this might be the result of the strong atmospheric warming during the GDS, which causes the hygropause to ascend to higher altitudes. The HDO/H_2O ratio is relatively stable before and during the GDS, which demonstrates that HDO is advected along with H_2O to higher altitudes and latitudes during the onset of the GDS.

Fractionation of HDO and H_2O is expected to occur during condensation of both isotopologues[33]. Model studies predict that through condensation and cloud sedimentation, the abundances of H_2O and HDO become very small above the hygropause[4,33]. This is confirmed by our first results (Fig. 3). The coincidence of a strong decrease in HDO, below detectability, with an observed water-ice cloud may provide the first direct indication of the fractionation process. Because of the fractionation effect, HDO is expected to be more concentrated inside the ice cloud and thus more scavenged from the condensation level, such that the HDO/H_2O ratio is expected to decrease with altitude. The effect of the dust storm is to expand the atmosphere and to lift the hygropause. Continued TGO measurements will permit us to unveil both the spatial and the seasonal trends of D/H.

Online content

Any methods, additional references, Nature Research reporting summaries, source data, statements of data availability and associated accession codes are available at https://doi.org/10.1038/s41586-019-1097-3.

1. Shirley, J. H., Newman, C., Mischna, M. & Richardson, M. Replication of the historic record of Martian global dust storm occurrence in an atmospheric general circulation model. *Icarus* **317**, 197–208 (2019).
2. Montabone, L. et al. Eight-year climatology of dust optical depth on Mars. *Icarus* **251**, 65–95 (2015).
3. Haberle, R. M., Clancy, R. T., Forget, F., Smith, M. D. & Zurek, R. W. *The Atmosphere and Climate of Mars* (Cambridge Univ. Press, Cambridge, 2017).
4. Daerden, F. et al. Mars atmospheric chemistry simulations with the GEM-Mars general circulation model. *Icarus* https://doi.org/10.1016/j.icarus.2019.02.030 (in the press).
5. Fedorova, A. et al. Water vapor in the middle atmosphere of Mars during the 2007 global dust storm. *Icarus* **300**, 440–457 (2018).
6. Heavens, N. G. et al. Hydrogen escape from Mars enhanced by deep convection in dust storms. *Nat. Astron.* **2**, 126–132 (2018).
7. Smith, M., Daerden, F., Neary, L. & Khayat, A. The climatology of carbon monoxide and interannual variation of water vapor on Mars as observed by CRISM and modeled by the GEM-Mars general circulation model. *Icarus* **301**, 117–131 (2018).
8. Trokhimovskiy, A. et al. Mars' water vapor mapping by the SPICAM IR spectrometer: five Martian years of observations. *Icarus* **251**, 50–64 (2015).
9. Sanchez-Lavega, A. et al. The 2018 Martian global dust storm over the south pole studied with VMC onboard Mars Express. *AGU Fall Meeting 2018*, abstr. P43K-3885 (2018).
10. Schofield, J., Kleinböhl, A., Kass, D. M. & McCleese, D. The Mars Climate Sounder – six Martian years of global atmospheric observations. In *42nd COSPAR Scientific Meeting* abstr. B4.1-0002-18 (2018).
11. Smith, M. D. THEMIS observations of Mars planet-encircling dust storm 2018a. In *AGU Fall Meeting 2018* abstr. P43J-3865 (2018).
12. Vasavada, A. Contributions of the Curiosity rover to the understanding of the Martian atmosphere. In *42nd COSPAR Scientific Meeting* abstr. C3.1-0008-18 (2018).
13. Guzewich, S., Talaat, E., Toigo, A., Waugh, D. W. & McConnochie, T. High-altitude dust layers on Mars: observations with the thermal emission spectrometer. *J. Geophys. Res. Planets* **118**, 1177–1194 (2013).
14. Heavens, N. G. et al. Seasonal and diurnal variability of detached dust layers in the tropical Martian atmosphere. *J. Geophys. Res. Planets* **119**, 1748–1774 (2014).
15. Määttänen, A. et al. A complete climatology of the aerosol vertical distribution on Mars from MEx/SPICAM UV solar occultations. *Icarus* **223**, 892–941 (2013).
16. Wang, C. et al. Parameterization of rocket dust storms on Mars in the LMD Martian GCM: modeling details and validation. *J. Geophys. Res.* **123**, 982–1000 (2018).
17. Rafkin, S. The potential importance of non-local, deep transport on the energetics, momentum, chemistry, and aerosol distributions in the atmospheres of Earth, Mars, and Titan. *Planet. Space Sci.* **60**, 147–154 (2012).
18. Spiga, A., Faure, J., Madeleine, J. B., Määttänen, A. & Forget, F. Rocket dust storms and detached dust layers in the Martian atmosphere. *J. Geophys. Res.* **118**, 746–767 (2013).
19. Daerden, F. et al. A solar escalator on Mars: self-lifting of dust layers by radiative heating. *Geophys. Res. Lett.* **42**, 7319–7326 (2015).
20. Clancy, R. T. et al. Extension of atmospheric dust loading to high altitudes during the 2001 Mars dust storm: MGS TES limb observations. *Icarus* **207**, 98–109 (2010).
21. Sefton-Nash, E. et al. Climatology and first-order composition estimates of mesospheric clouds from Mars Climate Sounder limb spectra. *Icarus* **222**, 342–356 (2013).
22. McCleese, D. J. et al. Structure and dynamics of the Martian lower and middle atmosphere as observed by the Mars Climate Sounder: seasonal variations in zonal mean temperature, dust, and water ice aerosols. *J. Geophys. Res.* **115**, E12016 (2010).
23. Chaffin, M. S., Deighan, J., Schneider, N. M. & Stewart, A. I. F. Elevated atmospheric escape of atomic hydrogen from Mars induced by high-altitude water. *Nat. Geosci.* **10**, 174–178 (2017).
24. Forget, F. et al. Improved general circulation models of the Martian atmosphere from the surface to above 80 km. *J. Geophys. Res.* **104**, 24155–24175 (1999).
25. Neary, L. & Daerden, F. The GEM-Mars general circulation model for Mars: description and evaluation. *Icarus* **300**, 458–476 (2018).
26. Steele, L. et al. The seasonal cycle of water vapour on Mars from assimilation of Thermal Emission Spectrometer data. *Icarus* **237**, 97–115 (2014).
27. Lewis, S. R. et al. The solsticial pause on Mars: 1. A planetary wave reanalysis. *Icarus* **264**, 456–464 (2016).
28. Lammer, H. et al. Outgassing history and escape of the martian atmosphere and water inventory. *Space Sci. Rev.* **174**, 113–154 (2013).
29. Encrenaz, T. et al. New measurements of D/H on Mars using EXES aboard SOFIA. *Astron. Astrophys.* **612**, A112 (2018).
30. Aoki, S. et al. Seasonal variation of the HDO/H_2O ratio in the atmosphere of Mars at the middle of northern spring and beginning of northern summer. *Icarus* **260**, 7–22 (2015).
31. Villanueva, G. et al. Strong water isotopic anomalies in the martian atmosphere: probing current and ancient reservoirs. *Science* **348**, 218–221 (2015).
32. Webster, C. R. et al. Isotope ratios of H, C and O in CO_2 and H_2O of the martian atmosphere. *Science* **341**, 260–263 (2013).
33. Montmessin, F., Fouchet, T. & Forget, F. Modeling the annual cycle of HDO in the Martian atmosphere. *J. Geophys. Res.* **110**, E03006 (2005).

NOMAD Science Team

Ann Carine Vandaele[1], Jose-Juan López-Moreno[4], Giancarlo Bellucci[3], Manish R. Patel[14], Gustavo Alonso-Rodrigo[21], Shohei Aoki[1], Francesca Altieri[3], Sophie Bauduin[22], David Bolsée[1], Giacomo Carrozzo[3], R. Todd Clancy[8], Edward Cloutis[9], Matteo Crismani[5], Frank Daerden[1], Fabiana Da Pieve[1], Emiliano D'Aversa[3], Cédric Depiesse[1], Justin T. Erwin[1], Giuseppe Etiope[3,23,24], Anna A. Fedorova[2], Bernd Funke[4], Didier Fussen[1], Maia Garcia-Comas[4], Anna Geminale[3], Jean-Claude Gérard[10], Marco Giuranna[3], Leo Gkouvelis[10], Francisco Gonzalez-Galindo[4], James Holmes[14], Benoît Hubert[10], Nicolay I. Ignatiev[2], Jacek Kaminski[12], Ozgur Karatekin[13], Yasumasa Kasaba[25], David Kass[26], Armin Kleinböhl[26], Orietta Lanciano[27], Franck Lefèvre[6], Stephen Lewis[14], Giuliano Liuzzi[5], Manuel López-Puertas[4], Miguel López-Valverde[4], Arnaud Mahieux[1], Jon Mason[14], Michael J. Mumma[5], Hiromu Nakagawa[25], Lori Neary[1], Eddy Neefs[1], Robert E. Novak[5], Fabrizio Oliva[3], Arianna Piccialli[1], Etienne Renotte[28], Birgit Ritter[10,13], Séverine Robert[1], Frédéric Schmidt[15], Nick Schneider[29], Giuseppe Sindoni[27], Michael D. Smith[5], Nicholas A. Teanby[16], Ed Thiemann[29], Ian R. Thomas[1], Alexander Trokhimovskiy[2], Loïc Trompet[1], Jean Vander Auwera[22], Geronimo Villanueva[5], Sébastien Viscardy[1], James Whiteway[17], Valerie Wilquet[1], Yannick Willame[1], Michael J. Wolff[8], Paulina Wolkenberg[3] & Roger Yelle[30]

ACS Science Team

Juan Alday[7], Francesca Altieri[3], Konstantin Anufreychik[2], Gabriele Arnold[31], Lucio Baggio[6], Denis A. Belyaev[2], Jean-Loup Bertaux[2,6], Natalia Duxbury[32], Anna A. Fedorova[2], François Forget[18], Thierry Fouchet[33], Davide Grassi[3], Alexey V. Grigoriev[2], Sandrine Guerlet[18], Paul Hartogh[34], Nikolay I. Ignatiev[2], Yasumasa Kasaba[25], Igor Khatuntsev[2], Nikita Kokonkov[2], Oleg Korablev[2], Vladimir Krasnopolsky[35,36], Ruslan Kuzmin[2,37], Gaétan Lacombe[6], Franck Lefèvre[6], Emmanuel Lellouch[33], Miguel López-Valverde[4], Igor Maslov[2], Mikhail Luginin[2], Anni Määttänen[6], Emmanuel Marcq[6], Javier Martin-Torres[38,39], Alexander Medvedev[34], Ehouarn Millour[18], Franck Montmessin[6], Boris Moshkin[2], Kevin S. Olsen[6], Manish R. Patel[14], Andrey Patrakeev[2], Dmitry Patsaev[2], Cathy Quantin-Nataf[40], Daniel Rodionov[2], Alexander Rodin[36], Alexey Shakun[2], Valery Shematovich[41], Ian R. Thomas[1], Nicolas Thomas[42], Alexander Trokhimovsky[2], Luis Vazquez[43], Matthieu Vincendon[44], Valérie Wilquet[1], Colin F. Wilson[7], Roland Young[18], Ludmila Zasova[2], Lev Zelenyi[2] & Maria Paz Zorzano[45]

[21]Instituto Universitario de Microgravedad, Universidad Politécnica de Madrid (IDR-UPM), Madrid, Spain. [22]Université Libre de Bruxelles, Brussels, Belgium. [23]Istituto Nazionale di Geofisica e Vulcanologia, Rome, Italy. [24]Faculty of Environmental Science and Engineering, Babes-Bolyai University, Cluj-Napoca, Romania. [25]Tohoku University, Sendai, Japan. [26]Jet Propulsion Laboratory, California Institute of Technology, Pasadena, CA, USA. [27]Agenzia Spaziale Italiana (ASI), Rome, Italy. [28]Advanced Mechanical and Optical Systems (AMOS), Liège, Belgium. [29]Laboratory for Atmospheric and Space Physics (LASP), Boulder, CO, USA. [30]Lunar and Planetary Laboratory (LPL), University of Arizona, Tucson, AZ, USA. [31]Deutsches Zentrum für Luft- und Raumfahrt (DLR), Institute of Planetary Research, Berlin, Germany. [32]Moscow University, Moscow, Russia. [33]Laboratoire d'études spatiales et d'instrumentation en astrophysique (LESIA), Observatoire de Paris-Meudon, Paris, France. [34]Max Planck Institute, Göttingen, Germany. [35]Catholic University of America, Washington, DC, USA. [36]School of Fundamental and Applied Physics, Moscow Institute of Physics and Technology (MIPT), Moscow, Russia. [37]Vernadsky Institute, Russian Academy of Sciences (RAS), Moscow, Russia. [38]Luleå University of Technology, Luleå, Sweden. [39]Instituto Andaluz de Ciencias de la Tierra, Universidad de Granada, Granada, Spain. [40]Laboratoire de Géologie de Lyon, Université Claude Bernard, Lyon, France. [41]Institute of Astronomy, Russian Academy of Sciences (RAS), Moscow, Russia. [42]University of Bern, Bern, Switzerland. [43]Universidad Complutense de Madrid, Madrid, Spain. [44]Institut d'Astrophysique Spatiale, Université Paris Sud, Orsay, France. [45]Centro de Astrobiología, Instituto Nacional de Técnica Aeroespacial (CSIC/INTA), Madrid, Spain.

METHODS

The NOMAD instrument and dataset. NOMAD, the Nadir and Occultation for MArs Discovery spectrometer suite[34–36], is part of the payload of the ExoMars 2016 Trace Gas Orbiter mission[37]. The instrument is conducting a spectroscopic survey of Mars' atmosphere in ultraviolet, visible and infrared wavelengths, covering large parts of the spectral range 0.2–4.3 μm. NOMAD is composed of three spectrometers: a solar-occultation-only spectrometer (SO) operating in the infrared (2.3–4.3 μm), a second infrared spectrometer (2.3–3.8 μm) capable of nadir, solar occultation and limb observations (LNO, Limb Nadir and solar Occultation) and an ultraviolet/visible spectrometer (UVIS; 200–650 nm) that also has all three observation modes. The spectral resolution of SO (0.15 cm^{-1} at 3,000 cm^{-1}) surpasses those of previous surveys from orbit in the infrared by at least one order of magnitude. NOMAD offers an integrated instrument combining a flight-proven concept and innovations based on existing instrumentation: SO is a copy of the SOIR (Solar Occultation in the InfraRed) instrument[38] on Venus Express (VEx)[39], LNO is a modified version of SOIR, and UVIS has heritage from the development of the Humboldt lander. NOMAD provides vertical profiling for atmospheric constituents at unprecedented spatial and temporal resolution. Indeed, in solar occultation, the vertical resolution is less than 1 km for SO and UVIS, with a sampling rate of 1 s (one measurement every 1 km), and occultations range from the surface to 200 km altitude. NOMAD also provides mapping of several constituents in nadir mode with an instantaneous footprint of 0.5×17 km^2 (LNO spectrometer) and 5 km^2 (UVIS spectrometer) at a repetition rate of 30 Martian days.

For this work we analysed SO channel data measured between 21 April and 30 September 2018. SO measures four spectra for five or six different diffraction orders per second in solar occultation mode.

The ACS instrument and dataset. The ACS[40] (Atmospheric Chemistry Suite) spectrometer consists of three infrared channels featuring high accuracy, high resolving power and a broad spectral coverage (0.7–17 μm). The near-infrared (NIR) channel is based on the principle of the echelle spectrometer, with selection of diffraction orders by an acousto-optical tuneable filter (AOTF). The same principle was employed by SOIR on VEx[38] and by the infrared channels of NOMAD described above. ACS NIR covers the spectral range 0.7–1.7 μm in diffraction orders 101 through 49. The instrument capitalizes on the science heritage of SPICAM-IR[41] onboard ESA's Mars Express, benefiting from a much higher resolving power of $\lambda/\Delta\lambda \approx 25,000$ (λ, wavelength). During an occultation, ACS NIR measures 10 preselected diffraction orders in two seconds, including the absorption bands of H$_2$O at 1.13, 1.38 and 1.40 μm and of CO$_2$ at 1.27, 1.43, 1.54 and 1.57 μm. The mid-infrared (MIR) channel is a newly developed cross-dispersion echelle spectrometer dedicated to solar occultation measurements in the 2.3–4.5-μm range. The spectral resolving power is $\lambda/\Delta\lambda \approx 50,000$. For each acquired frame, ACS MIR measures up to 20 adjacent diffraction orders, covering an instantaneous spectral range of 0.15–0.3 μm. To achieve the full spectral coverage, a secondary dispersion grating can be rotated to one out of 11 positions. The H$_2$O and HDO profiles can be measured simultaneously by ACS MIR using positions 4, 5 and 11.

The concept of the Fourier-transform spectrometer TIRVIM is similar to that of the Planetary Fourier Spectrometer (PFS)[42] onboard MEx, although TIRVIM features a cryogenic detector and solar occultation capability. In occultation, TIRVIM is operated mostly in 'climatology' mode, covering instantaneously (every 0.4 s) the full spectral range of 1.7–17 μm (effectively 1.7–5 μm) with spectral resolution ≤1 cm^{-1}. The three ACS channels are used to observe in solar occultation mode; ACS NIR and TIRVIM are operated also in nadir mode to measure atmospheric gases and to characterize the atmospheric state, namely, dust loading and condensation clouds. The atmospheric temperature profile is retrieved from the 15-μm CO$_2$ band measured by TIRVIM in nadir.

In this work we used ACS NIR occultation profiles (Fig. 2) obtained at high latitudes in the southern and northern hemispheres (see Extended Data Table 1). Simultaneous H$_2$O and HDO profiles (Fig. 3) were obtained with ACS MIR in the southern hemisphere in order 224 (position 4 of secondary grating). TIRVIM aerosol profiling (Extended Data Fig. 7) was done using solar occultation data obtained in the southern hemisphere, orbit 2556, $L_s = 197°$ and latitude 81° S during the egress (local time 9:26); that is, during the same occultation as the ACS MIR results shown in Fig. 3.

Solar occultation technique. The solar occultation technique is a powerful way to gain information on the vertical structure of atmospheres. At sunset, the recording of spectra starts well before the occultation occurs (the solar spectrum outside the atmosphere is used for referencing) and continues until the line of sight crosses the planet. At sunrise, the recording of spectra continues well above the atmosphere to provide the corresponding reference. Transmittances are obtained by dividing the spectra measured through the atmosphere by the reference spectrum recorded outside the atmosphere[43]. In this way, transmittances become independent of instrumental characteristics, such as the absolute response or the ageing of the instrument, in particular of the detector. Such observations provide high-vertical-resolution (<1 km for NOMAD SO and ACS NIR and 2.0–2.5 km for

ACS MIR observations) profiles of the structure and composition of the atmosphere. ACS TIRVIM observes the full Sun disk during an occultation, resulting in a coarser vertical resolution (about 9 km).

Profiles of dust extinction. To calculate the extinction due to dust and/or clouds, it is necessary to remove the absorption lines of atmospheric gas species, leaving the background continuum. For the analysis here, diffraction order 121 of NOMAD SO was chosen because (1) this order is measured routinely, so it has high spatial/ temporal coverage and (2) it is relatively simple to remove the atmospheric absorption lines. A fourth-order polynomial is fitted to the data. The optical depths in Fig. 1 are inferred from the value of the continuum at the centre of the detector (pixel 160). The fitting algorithm fails at low and high altitudes, where either the absorption lines from molecular species are saturated or the signal is so low that it is effectively noise. Therefore, any spectra with transmittance >99.5% are assumed to have an optical depth of 0, and points with transmittance <0.5% are not plotted; hence the lines end abruptly at low altitudes when the optical depth becomes high. The observations in Fig. 1 are split into northern, southern and middle latitudes using the following criteria: greater than 60°, northern; between −70° and −50°, southern; and between −30° and +30°, middle latitudes. The tangent altitude is calculated as the shortest distance between the line of sight of the centre of the field of view and the MGM1025 areoid (that is, the Mars geoid)[44]. The latitude is the point on the areoid closest to the centre of the field of view, that is, the tangent point, at the mid-point of the solar occultation measurement. The characteristics of the individual vertical profiles of optical depth vary with latitude, as seen when optical depth is plotted versus latitude and Martian longitude (Extended Data Fig. 1).

To further investigate the impact of the dust storm, two orbits covering the same footprint and solar illumination conditions on Mars were considered; they were acquired by the nadir channel of NOMAD before (26 April) and during (11 July) the GDS. Extended Data Fig. 2 compares the dust radiance signature before and after the storm but, in contrast to Fig. 1, in a nadir geometry and in a different wavelength, at 2.3 μm. Comparison with radiative-transfer modelling suggests an increase by a factor of about 10 in opacity at 2.3 μm during the storm. We note also that the surface albedo features are obscured by the increase in the atmospheric dust load. The radiance variation with latitude is mainly dominated by the total albedo (surface and atmosphere) and solar zenith angle, which varies along the track. The radiative-transfer model includes multiple scattering and a layered atmosphere with pressure/temperature profiles from the LMD general circulation model (GCM)[45]. Further details on the radiative transfer model can be found in Villanueva et al.[46].

Vertical profiles of H$_2$O and HDO volume mixing ratio. The vertical profiles of the H$_2$O and HDO volume mixing ratios are investigated using the NOMAD dataset shown in Extended Data Table 1. These NOMAD spectra were taken in the northern hemisphere at the same local time (18:00). The NOMAD SO channel can record spectra for multiple diffraction orders during an occultation. The occultation performed on 7 May includes the measurements of diffraction order 168 (3,775.53–3,805.63 cm^{-1}) and order 136 (3,056.39–3,080.75 cm^{-1}), where strong H$_2$O lines are present, and of order 119 (2,674.34–2,695.65 cm^{-1}) with strong HDO lines. The occultation measurement on 20 June contains two diffraction orders for H$_2$O, orders 168 and 134 (3,011.44–3,035.44 cm^{-1}), and diffraction order 121 for HDO (2,719.28–2,740.96 cm^{-1}) (Extended Data Fig. 3).

We retrieved the H$_2$O volume mixing ratio using the whole spectral range of those diffraction orders to maximize the information content at every occultation tangent altitude. In this study, CO$_2$ and H$_2$O gas absorptions were included. The absorption coefficients of these gases are calculated with a line-by-line method using the water vapour line list for a CO$_2$-rich atmosphere for H$_2$O[47,48] and HITRAN 2016[49] for CO$_2$. The temperature, pressure and CO$_2$ volume mixing ratio are taken from the values predicted by GCMs for each altitude. The calculated synthetic spectra are convolved with a Gaussian function that corresponds to the spectral resolving power of the NOMAD SO channel (11,000–15,000). The final synthetic spectra are then built by considering an instrument model that comprises the effects of the AOTF and the grating (that is, Blaze function)[50]. The free parameters in the retrievals are the vertical profiles of the volume mixing ratio and the parameters of the polynomial function used to model the continuum of each spectrum. Retrievals are performed using an optimal-estimation approach[51] implemented in a Gauss–Newton iterative scheme. Extended Data Fig. 4 shows an example of the fitting results.

The water vapour profiles shown in Fig. 2 are retrieved from the ACS NIR spectra (see also Extended Data Table 1). Wavelength drift is corrected using the positions of gas-absorption lines. The spectra fitting and the profile retrieval follow the method described for the SPICAM MEx 1.38-μm band[5,52]. All of the altitudes of the profiles are fitted simultaneously (global fit) using a Levenberg–Marquardt iterative algorithm[53,54]. Tikhonov regularization is then applied, which is customary for vertical inversions, to smooth the profile. The uncertainty in the local number densities is given by the covariance matrix of the solution

errors. The water vapour abundances are retrieved from spectra acquired in diffraction order 56 (covering the 1.38-μm band, or 7,220–7,300 cm^{-1}). Extended Data Fig. 5 shows an example of the fitting results. The spectral line parameters for H_2O are taken from HITRAN 2016[49] with a correction coefficient for the CO_2-rich atmosphere[5]. The temperature and pressure for the radiative-transfer computations are taken from the MCD[45] GCM. To obtain the volume mixing ratio profiles of water vapour, the CO_2 density was retrieved from ACS NIR spectra in order 49, 6,320–6,390 cm^{-1}.

The vertical profiles of the H_2O and HDO volume mixing ratios from the ACS dataset (Fig. 3b, c) were obtained in the southern hemisphere at middle and high latitudes (Extended Data Table 1). During these observations ACS MIR channels recorded spectra at position 4 (diffraction orders 210–224). To obtain the H_2O and HDO density, order 224 (3,763–3,775 cm^{-1}) was used for both observations on 2 May and 20 June. We retrieved H_2O and HDO volume mixing ratios using several lines present in this diffraction order. The spectral line parameters for H_2O were taken from HITRAN 2016 with a correction coefficient for the CO_2 broadening[5]. The temperature and pressure for the radiative-transfer computations were taken from the MCD GCM[45]. The calculated synthetic spectra were convolved with a Gaussian function corresponding to the spectral resolving power of the ACS MIR channel (30,000–35,000).

For both NOMAD and ACS, the D/H values were obtained by dividing the HDO and H_2O densities retrieved at the same altitude. The D/H errors were calculated by the weighted average:

$$\mathrm{D/H_{error}} = [\mathrm{D/H}]\sqrt{\left(\frac{\mathrm{HDO_{error}}}{[\mathrm{HDO}]}\right)^2 + \left(\frac{\mathrm{H_2O_{error}}}{[\mathrm{H_2O}]}\right)^2}$$

where square brackets indicate density. Because the H_2O and HDO densities were retrieved independently and from different datasets (here different orders and different absorption lines), they are truly independent. Therefore the errors are non-correlated. The errors capture the instrumental systematic effects because they are based on the final χ^2.

Water-ice clouds. Extended Data Fig. 6 shows the aerosol optical depth derived from NOMAD SO on 7 May 2018, before the dust storm, during which orders 119, 136, 148, 168 and 189 were measured, corresponding to central wavenumbers of 2,685.0, 3,068.0, 3,339.0, 3,790.0 and 4,265.0 cm^{-1}, respectively. The optical depths were derived by averaging the transmittances with a sampling interval of 3 km and deriving for each tangent height the equivalent optical depth rescaled by the occultation path. Each optical depth was determined simultaneously with the abundances of the other gases detectable in each order; hence a full retrieval was used. Each spectrum was processed with the planetary spectrum generator (PSG)[46] forward model and a retrieval scheme based on optimal estimation in a Gauss–Newton iterative scheme. The optical depth was derived for each single sampled altitude and compared to the extinction of water ice with different particle sizes (top panel in Extended Data Fig. 6). Extended Data Fig. 6 shows that the detached layer observed by NOMAD at 40–50 km is a water-ice cloud with particle sizes of 0.1–1 μm.

Aerosol properties from TIRVIM solar occultation data were retrieved from 20 wavenumbers in the spectral range of 1,500−4,500 cm^{-1}, chosen outside of strong-gas-absorption bands. This channel is operated continuously and therefore remains very stable during an occultation. To increase the signal-to-noise ratio, the spectra were averaged using the simple moving mean within a spectral window of 50 cm^{-1} centred at the chosen wavenumbers; spectral errors were calculated as s.e.m. with $n = 78$. The transmission and slant-optical-depth errors were calculated using propagation-of-uncertainty formulas. Vertical profiles of extinction and the corresponding errors were retrieved using the standard 'onion peeling' method described in Fedorova et al.[55]. Further steps involved Mie modelling of the spectral dependence of the extinction coefficient, assuming known optical properties for the aerosol[56,57] fits to the experimental data to retrieve vertical profiles of the size distribution and number density, as described in Fedorova et al.[58]. A logarithmic–normal size distribution[59] of the aerosol particles with a width (effective variance) of 0.3 was assumed. To distinguish between water-ice and dust particles, we applied the optimal-estimation retrieval scheme independently for both types and made the decision based on the fit quality (Extended Data Fig. 7). The algorithm was able to retrieve the number density (typically about one particle per cubic centimetre) and the effective radius (1–1.5 μm). Errors on these values were estimated from the covariance matrix.

Data availability

The datasets generated by the NOMAD and ACS instruments and analysed in this study will be available in the ESA PSA repository, https://archives.esac.esa.int/psa, after the proprietary period. The datasets used directly in this study, including the data used for the figures, are available from the corresponding author upon reasonable request.

Code availability

The codes used to calculate the dust/aerosol optical depths shown in Fig. 1 are available upon request from the corresponding author. The code used to inverse the NOMAD and ACS spectra and derive density profiles has been favourably compared to the PSG tool, which can be accessed at https://psg.gsfc.nasa.gov/ and which is part of this study. A version of the retrieval code is available at https://psg.gsfc.nasa.gov/helpatm.php#retrieval.

34. Vandaele, A. C. et al. NOMAD, an integrated suite of three spectrometers for the ExoMars Trace Gas mission: technical description, science objectives and expected performance. *Space Sci. Rev.* **214**, 80 (2018).
35. Neefs, E. et al. NOMAD spectrometer on the ExoMars trace gas orbiter mission: part 1—design, manufacturing and testing of the infrared channels. *Appl. Opt.* **54**, 8494–8520 (2015).
36. Patel, M. R. et al. The NOMAD spectrometer on the ExoMars Trace Gas Orbiter mission: part 2—design, manufacturing and testing of the ultraviolet and visible channel. *Appl. Opt.* **56**, 2771–2782 (2017).
37. Svedhem, H. et al. The ExoMars Trace Gas Orbiter. *Space Sci. Rev.* (in the press).
38. Nevejans, D. et al. Compact high-resolution spaceborne echelle grating spectrometer with acousto-optical tunable filter based on order sorting for the infrared domain from 2.2 to 4.3 μm. *Appl. Opt.* **45**, 5191–5206 (2006).
39. Titov, D. V. et al. Venus Express: scientific goals, instrumentation and scenario of the mission. *Cosm. Res.* **44**, 334–348 (2006).
40. Korablev, O. et al. The Atmospheric Chemistry Suite (ACS) of three spectrometers for the ExoMars 2016 Trace Gas Orbiter. *Space Sci. Rev.* **214**, 7 (2018).
41. Korablev, O. et al. SPICAM IR acousto-optic spectrometer experiment on Mars Express. *J. Geophys. Res.* **111**, E09S03 (2006).
42. Formisano, V. et al. The Planetary Fourier Spectrometer (PFS) onboard the European Mars Express mission. *Planet. Space Sci.* **53**, 963–974 (2005).
43. Trompet, L. et al. Improved algorithm for the transmittance estimation of spectra obtained with SOIR/Venus Express. *Appl. Opt.* **55**, 9275–9281 (2016).
44. Lemoine, F. G. et al. An improved solution of the gravity field of Mars (GMM-2B) from Mars Global Surveyor. *J. Geophys. Res.* **106**, 23359-23376 (2001).
45. Millour, E. et al. The Mars Climate Database (MCD version 5.2). *European Planetary Science Congress 2015*, abstr. EPSC2015-43810 (2015).
46. Villanueva, G., Smith, M., Protopapa, S., Faggi, S. & Mandell, A. M. Planetary Spectrum Generator: an accurate online radiative transfer suite for atmospheres, comets, small bodies and exoplanets. *J. Quant. Spectrosc. Radiat. Transf.* **217**, 86–104 (2018).
47. Devi, V. M. et al. Line parameters for CO_2- and self-broadening in the v_3 band of HD^{16}O. *J. Quant. Spectrosc. Radiat. Transf.* **203**, 158–174 (2017).
48. Devi, V. M. et al. Line parameters for CO_2- and self-broadening in the v_1 band of HD^{16}O. *J. Quant. Spectrosc. Radiat. Transf.* **203**, 133–157 (2017).
49. Gordon, I. E. et al. The HITRAN2016 molecular spectroscopic database. *J. Quant. Spectrosc. Radiat. Transf.* **203**, 3–69 (2017).
50. Liuzzi, G. et al. Methane on Mars: new insights into the sensitivity of CH_4 with the NOMAD/ExoMars spectrometer through its first in-flight calibration. *Icarus* **321**, 671–690 (2019).
51. Rodgers, C. D. *Inverse Methods for Atmospheric Sounding: Theory and Practice* (World Scientific, Singapore, 2000).
52. Maltagliati, L. et al. Annual survey of water vapor vertical distribution and water–aerosol coupling in the martian atmosphere observed by SPICAM/MEx solar occultations. *Icarus* **223**, 942–962 (2013).
53. Levenberg, K. A method for the solution of certain non-linear problems in least squares. *Q. J. Appl. Math.* **2**, 164–168 (1944).
54. Marquardt, D. An algorithm for least-squares estimation of nonlinear parameters. *J. Soc. Ind. Appl. Math.* **11**, 431–441 (1963).
55. Fedorova, A. et al. Solar infrared occultation observations by SPICAM experiment on Mars-Express: simultaneous measurements of the vertical distributions of H_2O, CO_2 and aerosol. *Icarus* **200**, 96–117 (2009).
56. Warren, S. G. & Brandt, R. E. Optical constants of ice from the ultraviolet to the microwave: a revised compilation. *J. Geophys. Res.* **113**, D14220 (2008).
57. Wolff, M. J. et al. Wavelength dependence of dust aerosol single scattering albedo as observed by CRISM. *J. Geophys. Res.* **114**, E00D04 (2009).
58. Fedorova, A. et al. Evidence for a bimodal size distribution for the suspended aerosol particles on Mars. *Icarus* **231**, 239–260 (2014).
59. Hansen, J. E. & Travis, L. D. Light scattering in planetary atmospheres. *Space Sci. Rev.* **16**, 527–610 (1974).
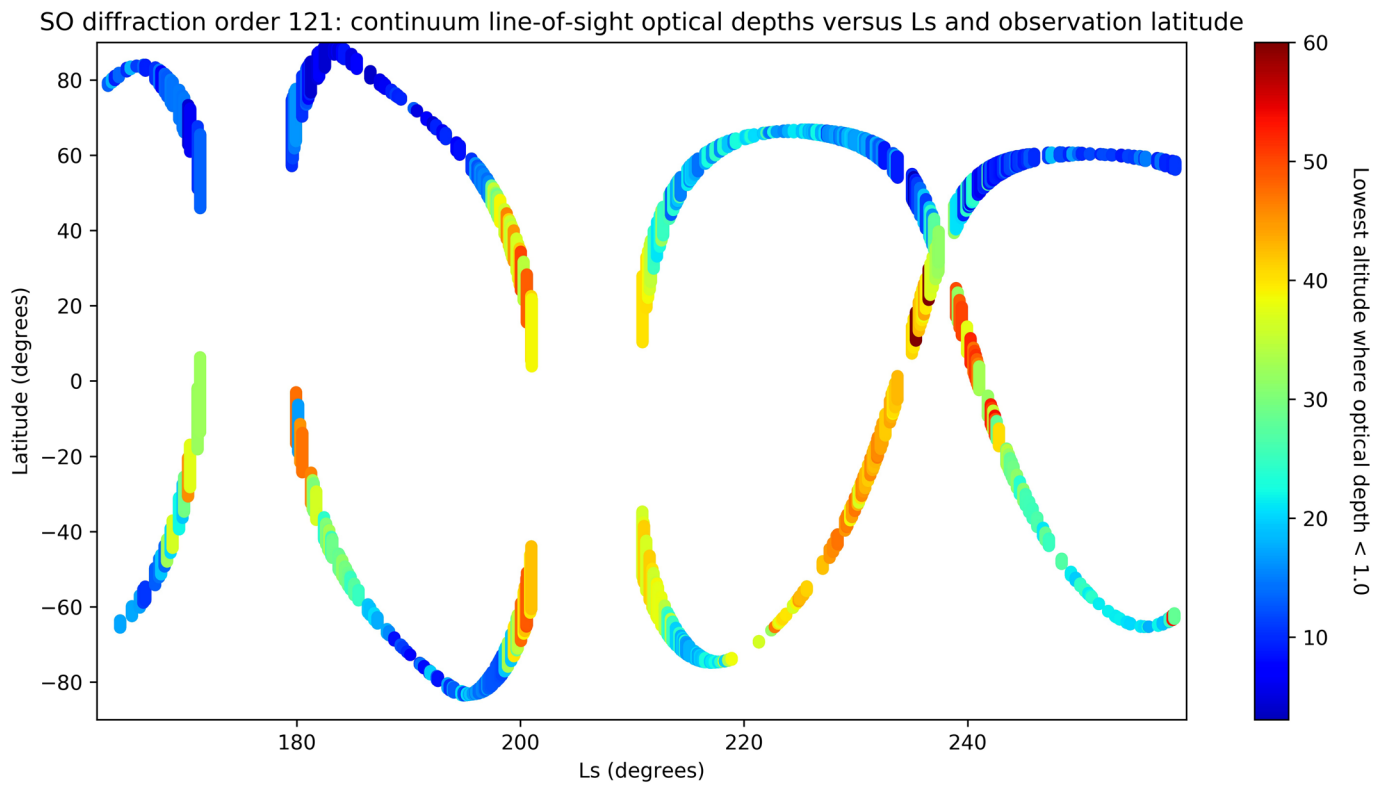
Extended Data Fig. 1 | Continuum optical depth versus latitude and solar longitude. The colour denotes the lowest altitude at which the optical depth is less than 1.0, that is, the lowest altitude where sunlight can still penetrate the atmosphere easily. There is a strong latitudinal dependence, with northern and southern high latitudes being relatively clear until the line of sight drops below 10–15 km (blue and dark blue)— except during the $L_s = 200°–240°$ period, where the GDS appears to have raised this altitude to 20–25 km (light blue and cyan).
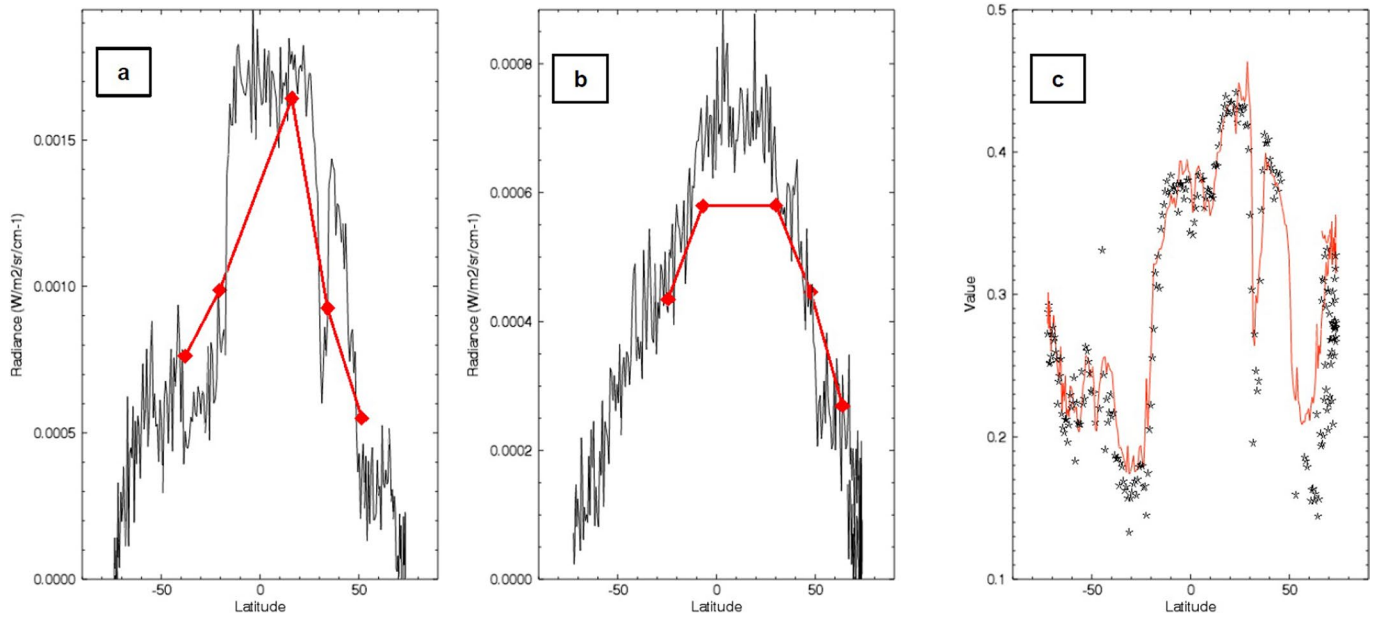
Extended Data Fig. 2 | Impact of the dust storm on NOMAD LNO nadir observations. a, **b**, The calibrated radiance at 2.3 μm is shown for two orbits, before (**a**) and during (**b**) the dust event, as a function of the latitude. Red lines show the results of a radiative-transfer model. The dust opacity before the GDS is $\tau = 0.46$ at 3 μm, whereas during the event

there is an increase by at least a factor of 10 ($\tau = 4.6$). The 1σ error of the data is 8.2×10^{-5} W m^{-2} sr^{-1} cm. **c**, Surface albedo. Black, albedo at 2.33 μm from the OMEGA/Mars Express instrument (corresponding to NOMAD order 190); red, bond albedo from the TES/Mars Global Surveyor instrument, scaled to the OMEGA one.
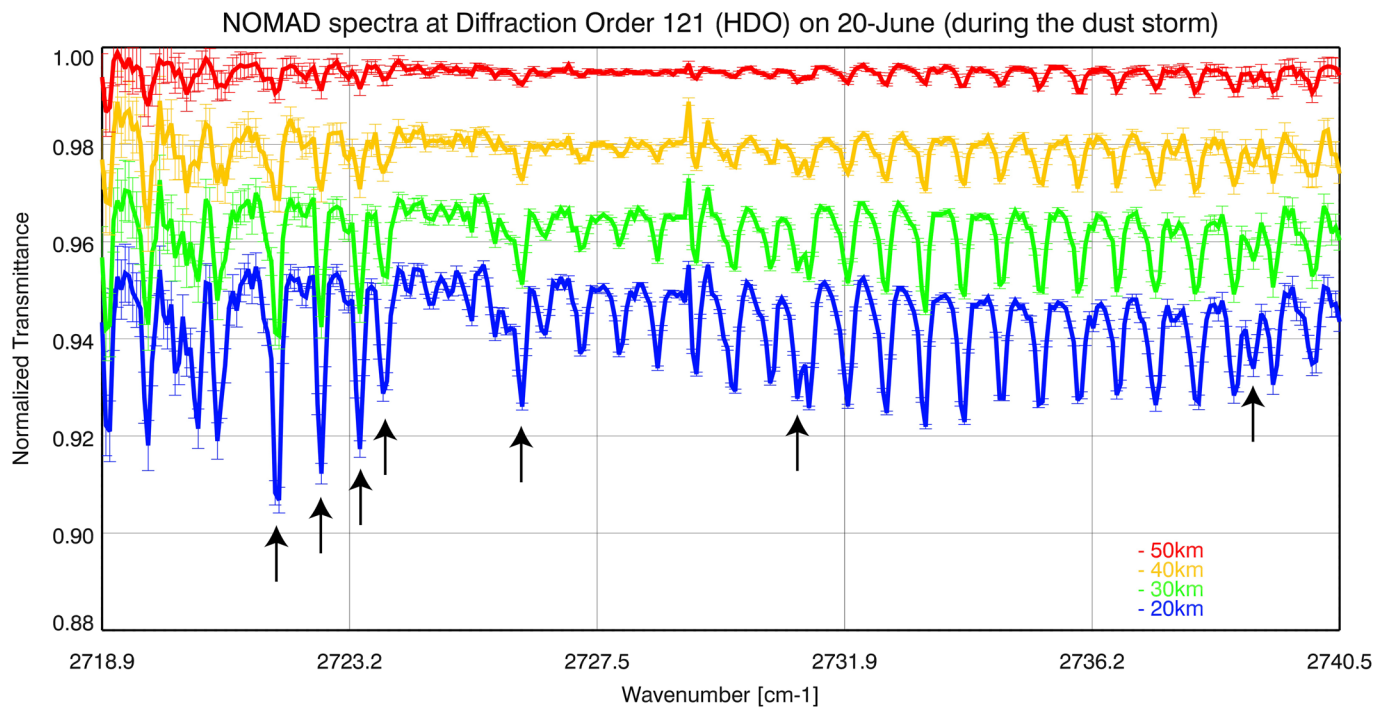
Extended Data Fig. 3 | Atmospheric transmittances measured by NOMAD during the storm. Data obtained at $L_s = 196.64°$, latitude 51° N and longitude 148° E, showing HDO absorption features (arrows) appearing at tangent heights of up to 50 km; most of the other absorption features originate from CO_2. The transmittances have been normalized by the continuum defined by a fifth-order polynomial applied to eliminate aerosol extinction and instrument effects. The transmittances are plotted with an interval of 0.015 to avoid overlapping.
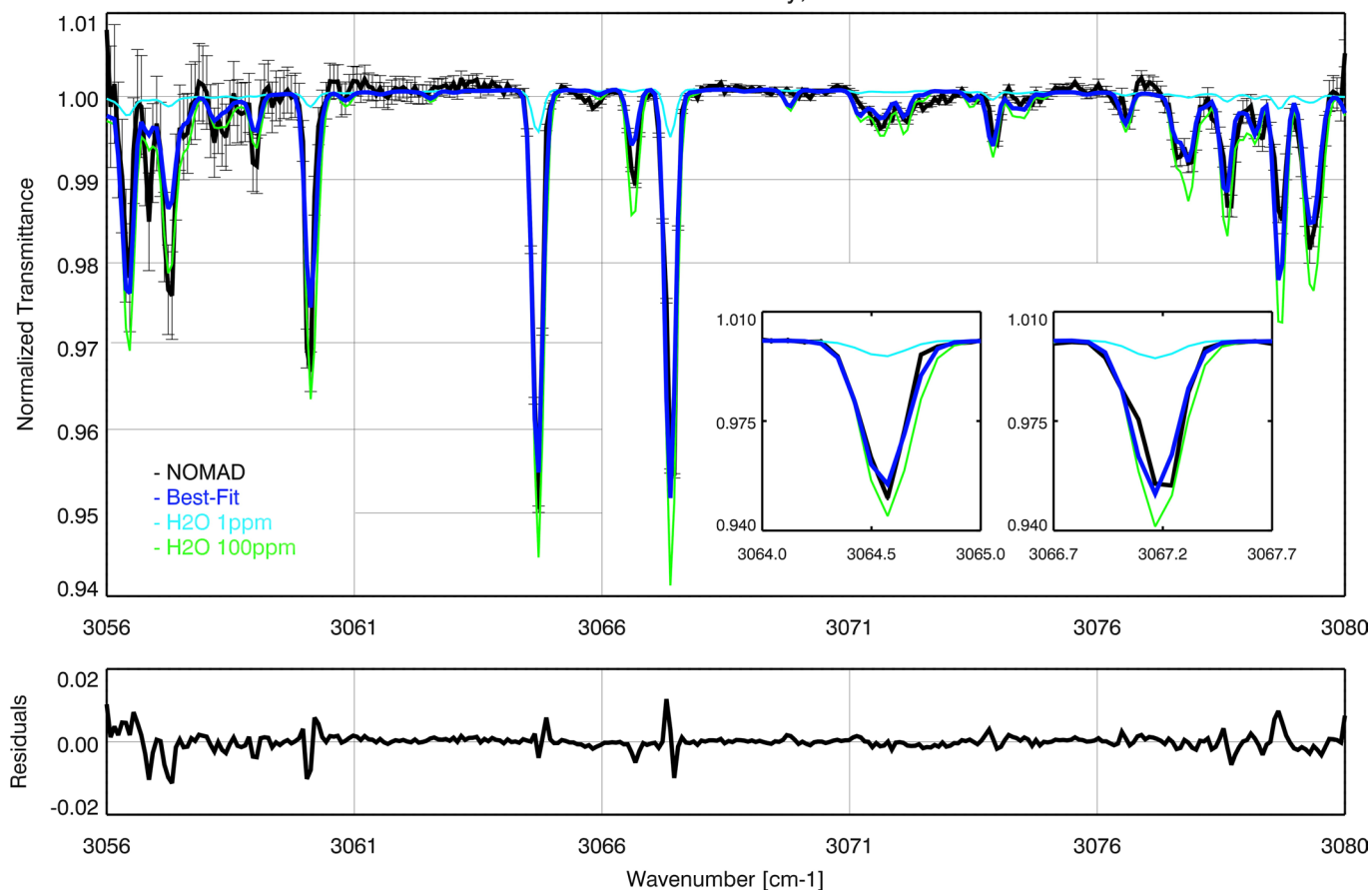
Extended Data Fig. 4 | Example of NOMAD water-retrieval results. Top, transmittance measured at a tangent height of 22.2 km (black), best fit (blue) and different simulations with 1 p.p.m. (cyan) and 100 p.p.m. (green) water content. The insets show zooms on two absorption lines of water. Bottom, residuals between the observation and the best fit. The transmittance errors were calculated from the 1σ noise value.
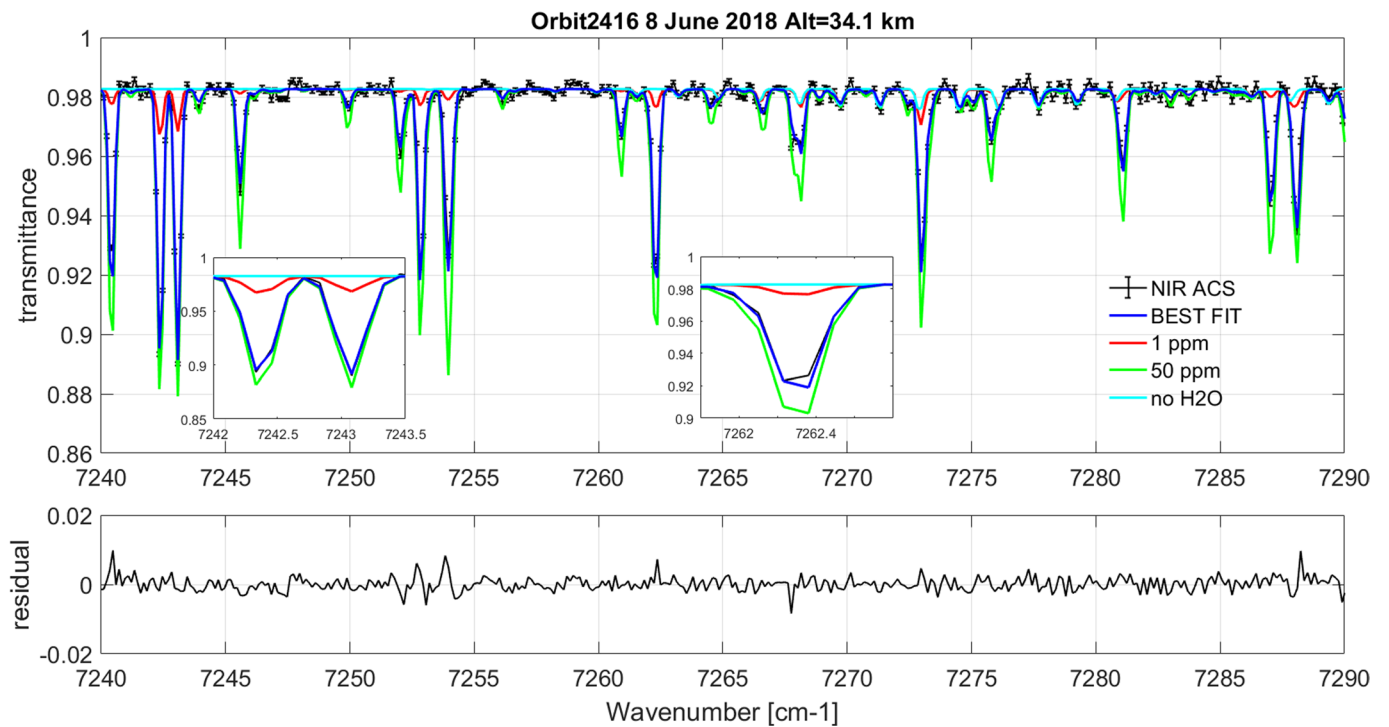
Extended Data Fig. 5 | Example of ACS NIR water-retrieval results. Top, transmittance measured at a tangent height of 34.1 km (black), best fit (blue) and different simulations with no water (cyan), 1 p.p.m. (red) and 50 p.p.m. (green) water content. The insets show zooms on several absorption lines of water. Bottom, residuals between the observation and the best fit. The transmittance errors were calculated from the 1σ noise value.
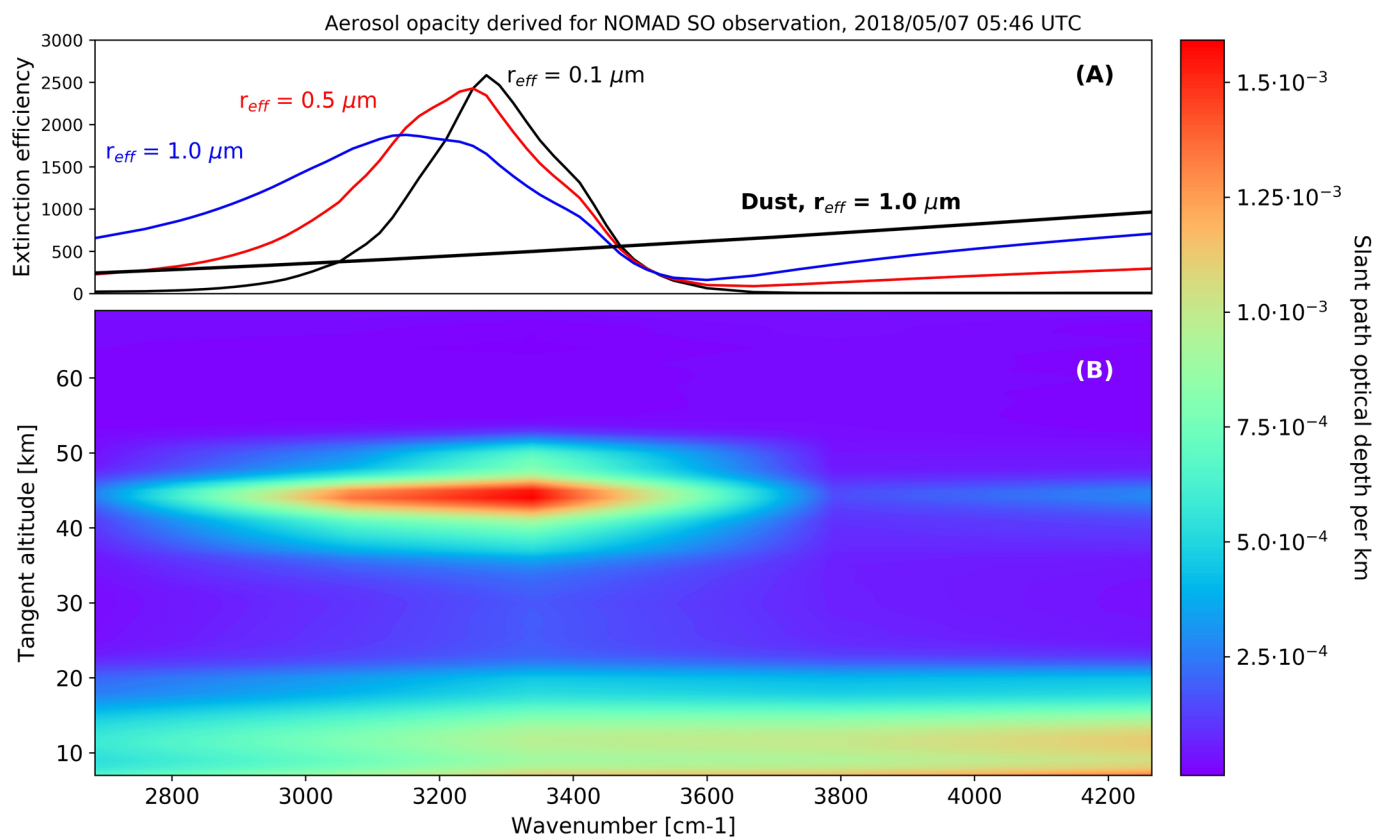
Extended Data Fig. 6 | Extinction of water ice measured by NOMAD.
Results shown as a function of particle size (retrieved effective radius, r_{eff}; top) and slant optical depth (in units of km^{-1}; bottom). Data obtained for the solar occultation before the dust storm, on 7 May between 05:40 and 05:46 UTC (local time 18:00), which covers the latitude range 44° N to 57° N and the longitude range −122.6° E to −121.4° E.
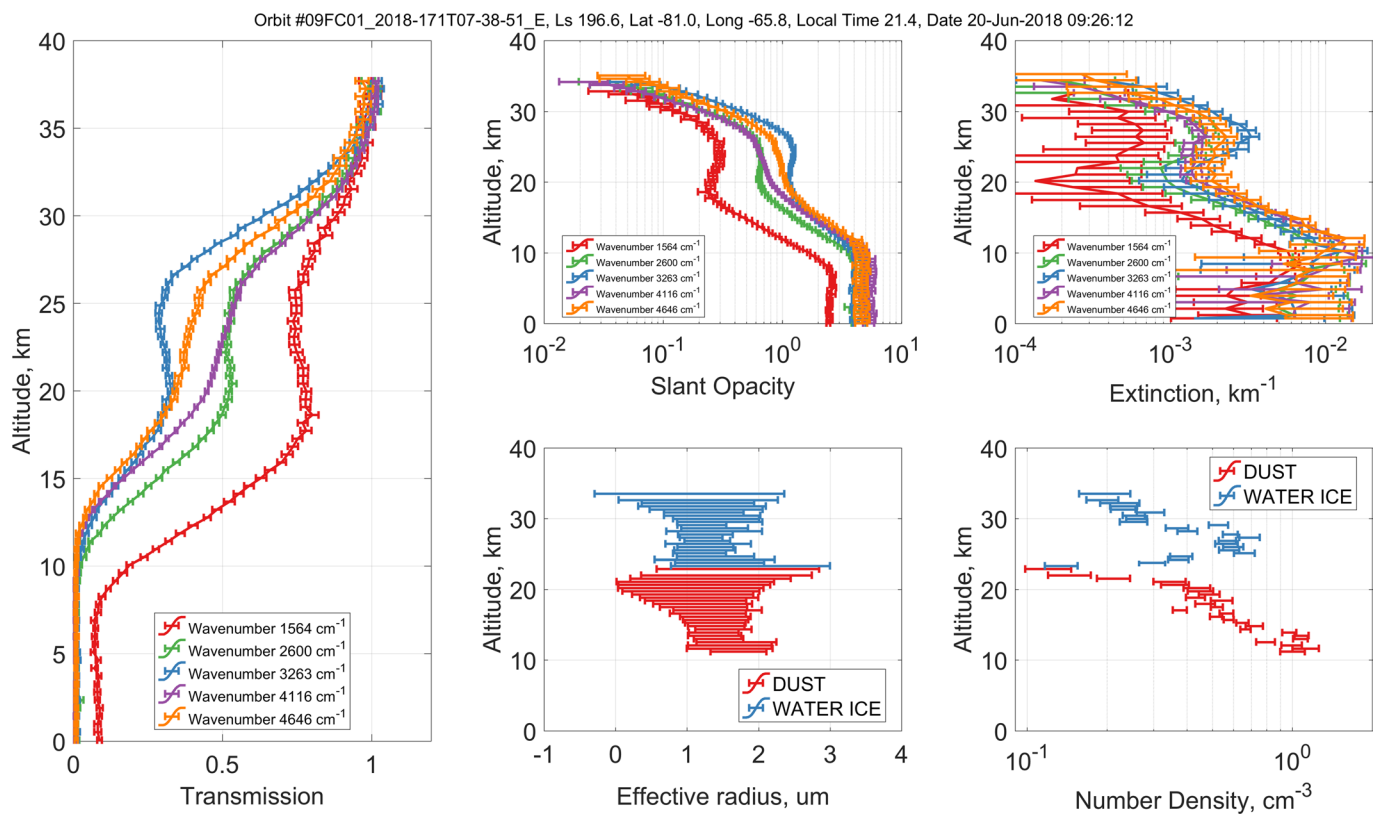
Extended Data Fig. 7 | Independent retrieval of dust and water ice from the TIRVIM dataset. Data obtained for a typical southern-hemisphere occultation (20 June 2018; latitude (Lat) 81° N; longitude (Lon) −66° E; egress). Shown is a selection of transmission profiles at five wavelengths (left), the corresponding slant opacities (top centre) and extinction profiles (top right), the retrieved effective radius r_{eff} (in micrometres; bottom centre) and the aerosol number density (in cm^{-3}; bottom right). The occultation measurement was performed at orbit 2556 (local time 21:25) and covers the latitude range 81° N to 82° N and the longitude range −67° E to −60° E. The observation corresponds to the ACS MIR H_2O and HDO profiles shown in Fig. 3 (yellow curves). The water ice and dust are well distinguished using the 3-μm water-ice absorption band (wavenumber 3,263 cm^{-1} in the figure). In this case the water-ice cloud is detected at 25–30 km. All errors shown are 1σ.

Extended Data Table 1 | Overview of NOMAD and ACS observations of H$_2$O and HDO used in this study

Instrument	Date (UT)	Solar Longitude	Latitude	East Longitude	Local solar time	Diffraction orders	Time relative to the Global Dust Storm
ACS-MIR	2 May 2018	168.75°	39°S - 43°S	156° - 157°	17.7	224 (H$_2$O), 224 (HDO)	Before
NOMAD SO	7 May 2018	171.45°	43° - 68° N	-122° - 115°	18.3	168 (H$_2$O), 136 (H$_2$O), 119 (HDO)	Before
ACS-NIR	6 June 2018	188.28°	77.5°N	-173°	16.8	56 NIR (H$_2$O)	Beginning
ACS-NIR	6 June 2018	188.62°	68.2°S	161.6°	5.4	56 NIR (H$_2$O)	Beginning
ACS-NIR	6 June 2018	188.75°	76.4°N	-100.5°	16.9	56 NIR (H$_2$O)	Beginning
ACS-NIR	7 June 2018	189.19°	70°S	176°	5.3	56 NIR (H$_2$O)	Beginning
ACS-NIR	7 June 2018	189.41°	74.8°N	-141.3°	17.0	56 NIR (H$_2$O)	Beginning
ACS-NIR	8 June 2018	189.67°	71.3°S	-112.3°	5.2	56 NIR (H$_2$O)	Beginning
ACS-NIR	8 June 2018	189.89°	73.8°N	-68°	17.0	56 NIR (H$_2$O)	Beginning
ACS-NIR	8 June 2018	190.05°	72.4°S	16.8°	5.1	56 NIR (H$_2$O)	Beginning
ACS-NIR	8 June 2018	190.52°	73.8°S	88.11°	4.9	56 NIR (H$_2$O)	Beginning
ACS-MIR-TIRVIM	20 June 2018	196.64°	80° S - 83°S	-68° - 52°	21.5	224 MIR (H$_2$O),224 MIR (HDO)	During
NOMAD SO	20 June 2018	196.64°	51° - 59° N	-148°	17.3	168 (H$_2$O),134 (H$_2$O), 121 (HDO)	During